Secondary magnetite in ancient zircon precludes analysis of a Hadean geodynamo

Secondary magnetite in ancient zircon precludes analysis of a Hadean geodynamo

Fengzai Tang[a], Richard J. M. Taylor[a,1], Josh F. Einsle[a,b], Cauê S. Borlina[c], Roger R. Fu[d], Benjamin P. Weiss[c], Helen M. Williams[a], Wyn Williams[e], Lesleis Nagy[f], Paul A. Midgley[b], Eduardo A. Lima[c], Elizabeth A. Bell[g], T. Mark Harrison[g], Ellen W. Alexander[g], and Richard J. Harrison[a]

[a]Department of Earth Sciences, University of Cambridge, CB2 3EQ Cambridge, United Kingdom; [b]Department of Materials Science and Metallurgy, University of Cambridge, CB2 3EQ Cambridge, United Kingdom; [c]Department of Earth, Atmospheric, and Planetary Sciences, Massachusetts Institute of Technology, Cambridge, MA 02139; [d]Department of Earth and Planetary Sciences, Harvard University, Cambridge, MA 02138; [e]School of Geosciences, University of Edinburgh, EH9 3FE Edinburgh, United Kingdom; [f]Geoscience Research Division, University of California, San Diego, La Jolla, CA 92093; and [g]Department of Earth, Planetary, and Space Sciences, University of California, Los Angeles, CA 90095

Edited by Donald J. DePaolo, Lawrence Berkeley National Laboratory, Berkeley, CA, and approved November 27, 2018 (received for review June 28, 2018)

Zircon crystals from the Jack Hills, Western Australia, are one of the few surviving mineralogical records of Earth's first 500 million years and have been proposed to contain a paleomagnetic record of the Hadean geodynamo. A prerequisite for the preservation of Hadean magnetization is the presence of primary magnetic inclusions within pristine igneous zircon. To date no images of the magnetic recorders within ancient zircon have been presented. Here we use high-resolution transmission electron microscopy to demonstrate that all observed inclusions are secondary features formed via two distinct mechanisms. Magnetite is produced via a pipe-diffusion mechanism whereby iron diffuses into radiation-damaged zircon along the cores of dislocations and is precipitated inside nanopores and also during low-temperature recrystallization of radiation-damaged zircon in the presence of an aqueous fluid. Although these magnetites can be recognized as secondary using transmission electron microscopy, they otherwise occur in regions that are indistinguishable from pristine igneous zircon and carry remanent magnetization that postdates the crystallization age by at least several hundred million years. Without microscopic evidence ruling out secondary magnetite, the paleomagnetic case for a Hadean–Eoarchean geodynamo cannot yet been made.

Hadean | paleomagnetism | Jack Hills | zircon | correlative microscopy

The earliest paleomagnetic evidence for an active geodynamo comes from circa (c.) 3.45-billion-year-old (Ga) rocks from the Barberton Greenstone Belt and the Pilbara Craton (1–3). According to many core formation models, the fields recorded by these rocks predate inner-core solidification, the process that powers the present-day geodynamo through the release of light elements at the inner-core/outer-core boundary. Before inner-core solidification, the geodynamo may have been powered by thermal convection alone. Recent upward revision of core thermal conductivity (4–6) means that high heat flux is needed to meet paleomagnetic constraints for a pure thermal dynamo. This leads to surprising predictions of a very young inner core (<600 Ma) and initial core temperatures that were hot enough to melt substantial portions of the lower mantle (7–9). As debate surrounding core thermal conductivity and implications for Earth's earliest magnetic fields continues (10), there is an ever-increasing need to place robust paleomagnetic constraints on the early geodynamo.

The lack of data before 3.45 Ga leaves a gap of over a billion years in the paleomagnetic record. Attempts to fill this gap have recently focused on the Jack Hills, Western Australia (11), where 2.65–3.05 Ga metaconglomerates contain detrital zircon grains with U–Pb ages as old as 4.4 Ga (12). Although zircon ($ZrSiO_4$) is not itself magnetic, zircon crystals contain inclusions of magnetic minerals that make them potential targets for single-crystal paleomagnetic analysis (13). Tarduno et al. (11) presented a single-crystal paleomagnetic study of Jack Hills detrital zircons, arguing that zircons dated between 3.3 and 4.2 Ga contain primary thermoremanent magnetization (TRM) imparted by an active Hadean to Paleoarchean geodynamo. No microscopy images of primary magnetic carriers within Jack Hills zircon have been presented to date. Rather, there is abundant evidence for secondary magnetic sources on surfaces, along internal cracks, around multiphase microgranite inclusions, and within metamict zones particularly for grains that have not been cleaned with HCl (14). Constraining the source of magnetization—and demonstrating the lack of interference by secondary remanence carriers (15)—is an essential step in confirming the robustness of Hadean paleomagnetism. To this end, we performed a direct study to determine the origin and setting of ferromagnetic carriers in Jack Hills zircon using correlative magnetic measurements and electron microscopy.

Zircon crystals were extracted from metaconglomerates of the Erawandoo Hill Hadean-zircon discovery outcrop (16, 17). We focus primarily on two grains (A and B) that are >3.9 Ga and that passed strict initial selection criteria for potential paleomagnetic targets: lack of evidence for alteration from scanning electron microscopy (SEM) images, concordant U–Pb ages (*SI Appendix*, section E), and treatment with 6M HCl to remove Fe in cracks (14), and a stable natural remanent magnetization (NRM) component (*SI Appendix*, section C). Three broadly defined textures are seen in SEM images: (*i*) primary oscillatory

Significance

The Earth's geodynamo is critical in protecting our atmosphere, and thus plays an important role in the habitability of our planet. As such, the Earth's magnetic field has likely played a crucial role in the emergence of life around 4 billion years ago during the Hadean–Archean Eons. However, we know little about the behavior of the geodynamo during this critical period. Recent efforts have focused on the magnetic signals harbored by Jack Hills zircon crystals, the oldest terrestrial material. Here we show the magnetic carriers in such grains. Our results demonstrate that although ancient zircon grains may contain ideal magnetic recorders, they do not record the magnetic field strength at the time of zircon growth.

Author contributions: R.J.M.T., J.F.E., B.P.W., H.M.W., W.W., P.A.M., T.M.H., and R.J.H. designed research; F.T., R.J.M.T., J.F.E., C.S.B., R.R.F., W.W., L.N., E.A.L., E.A.B., and E.W.A. performed research; W.W. and L.N. contributed new reagents/analytic tools; F.T., R.J.M.T., J.F.E., R.R.F., E.W.A., and R.J.H. analyzed data; and R.J.M.T. and R.J.H. wrote the paper.

The authors declare no conflict of interest.

This article is a PNAS Direct Submission.

[1]To whom correspondence should be addressed. Email: rjt79@cam.ac.uk.

This article contains supporting information online at www.pnas.org/lookup/suppl/doi:10.1073/pnas.1811074116/-/DCSupplemental.

Published online December 31, 2018.

zoning, (*ii*) recrystallized zones with bright cathodoluminescence (CL; grain B only), and (*iii*) strongly radiation-damaged metamict zones (individual oscillatory zones in grain A and the entire rim of grain B). Specific areas (Fig. 1) were targeted for scanning transmission electron microscopy (STEM) because of strong magnetic signals observed in the zircon interior using quantum diamond microscopy (QDM) (18). TEM lamellae were extracted from two grains targeting QDM signals within zones displaying primary oscillatory zoning (Fig. 1 *A* and *E*). Sample extraction was after thermal demagnetization experiments for grains A and B, but not for grain C (*SI Appendix*, *SI Appendix*, section A, and *SI Appendix*, Figs. S7–S11). Both heated and nonheated grains displayed identical features. Magnetic regions are observed in areas that display primary zoning and recrystallized zones. Additional images are available in *SI Appendix*, section A.

Grain A ($^{207}Pb^*/^{206}Pb^*$ age = 3979 Ma) clearly displays magnetic signals hosted by primary magmatic zoning in SEM images (Fig. 1 *A*–*D*). However, at the TEM scale, the lamella shows unequivocal microstructural evidence of partial recovery from radiation damage with clearly observed porosity and dislocations (Fig. 2 *A*–*C*). This fluid-absent lattice recovery leads to the formation of nanoscale pores that preferentially nucleate on dislocations, forming strings of pores linked by a common dislocation line that crosscuts primary zonation (Fig. 2*A*). Dislocation cores concentrate nonstructural elements such as Fe and provide fast pipe-diffusion pathways to deliver these elements from external sources to an internal sink (19–21). Direct evidence of this mechanism is seen during the earliest stages of infilling, where Fe accumulates at the intersection of the pore and the dislocation core (Fig. 2*F*). Pores are frequently partially or fully filled with precipitate phases such as magnetite, ilmenite ($FeTiO_3$), and crystalline ZrO_2 (potentially baddeleyite). The result is secondary, dislocation/pore-hosted, nanoscale magnetite grains within zircon that appears unaltered at SEM scale. No magnetite was found that does not lie on secondary microstructures, hence these observations demonstrate that all of the magnetite observed here postdates primary zircon crystallization. A comprehensive set of images of secondary magnetite and associated microstructures in grain A can be found in *SI Appendix*, Fig. S2.

Grain B ($^{207}Pb^*/^{206}Pb^*$ age = 3973 Ma) shows similar features to A in primary oscillatory zoned areas, along with an additional fluid-mediated recrystallization zone also hosting magnetic signals. Recrystallization proceeds as a diffusion–reaction process in which hydrous species diffuse inward and catalyze structural recovery (22, 23). We observe sinuous recrystallization fronts with bright CL, often closely associated with metamict areas that facilitate fluid ingress (Fig. 1*J* and *SI Appendix*, Fig. S5*A*). These recrystallized areas contain defect-rich crystalline zircon and crystallographically oriented precipitates of magnetite with elongated morphology due to preferential growth along intersecting dislocations (*SI Appendix*, Fig. S5*F*). These characteristics are typical of oxide inclusions precipitated from a silicate host by heterogeneous nucleation on dislocations (24, 25) and support a secondary origin for the magnetite in the recrystallized zones. A comprehensive set of images of secondary magnetite and associated microstructures

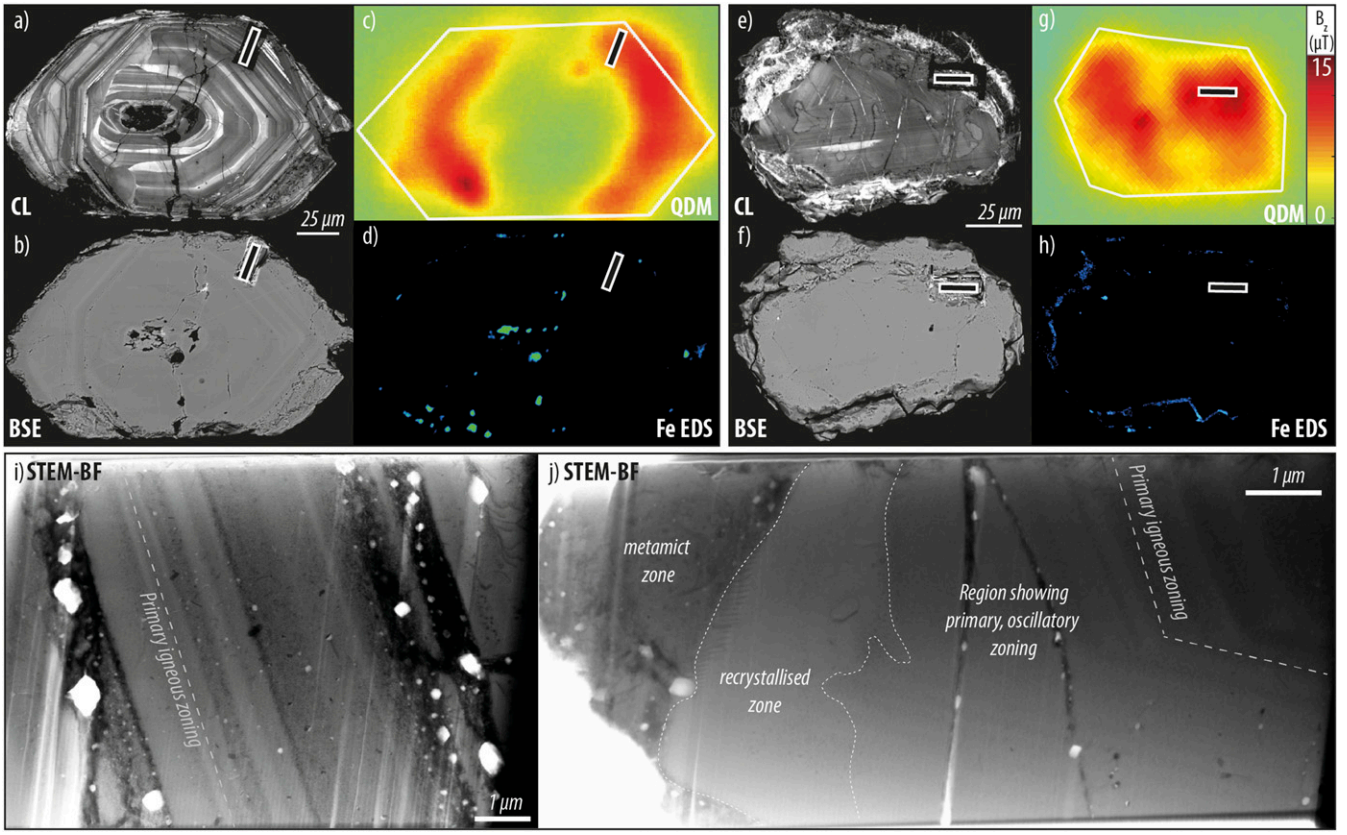

Fig. 1. Summary of SEM (*A*–*H*) and TEM (*I* and *J*) images of Jack Hills zircon grains A and B in this study. White outline rectangles mark original location of TEM lamellae. SEM—grain A: (*A*) CL image showing primary igneous zoning; (*B*) BSE image; (*C*) QDM magnetic anomaly map; and (*D*) compositional map of Fe intensity. Grain B: (*E*) CL image showing primary igneous zoning; (*F*) BSE image; (*G*) QDM magnetic anomaly map; and (*H*) compositional map of Fe intensity. Note that *E* and *F* were taken after a final polish, so that the TEM foil location appears less central than in *G*, which was taken before final polish. (*I*) TEM lamella showing primary zoning and associated secondary inclusions in grain A; and (*J*) TEM lamella showing primary zoning (RHS) and secondary inclusions in grain B. Metamict areas and a fluid-assisted recrystallization zone appear on the LHS. Color scale in *G* also applies to *C*.

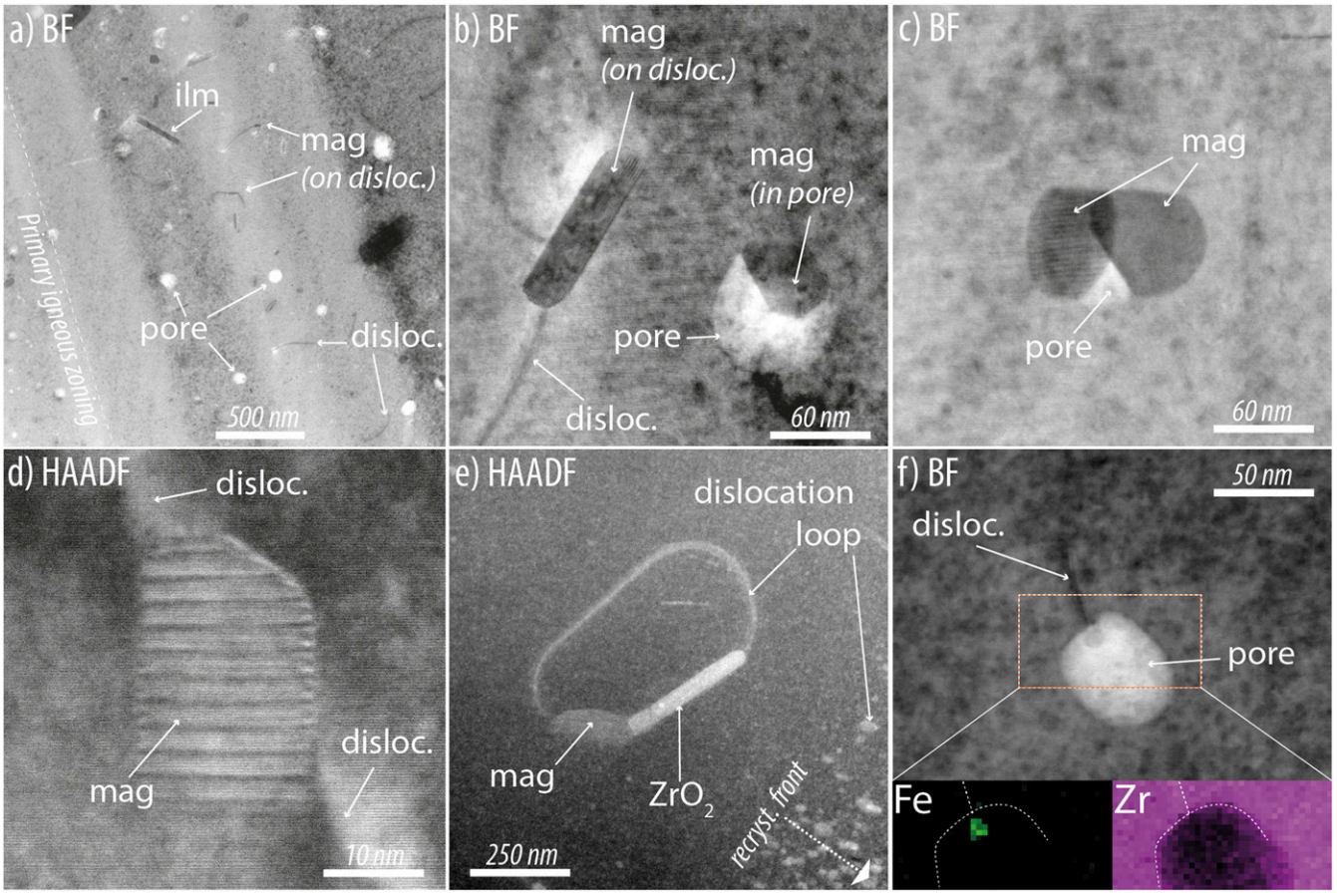

Fig. 2. High-resolution STEM images of nanoscale features and inclusions in this study. Background matrix is zircon. (*A*) Broad view of primary zoning with secondary features related to recovery of radiation damage. (*B*) Secondary magnetite grains along dislocations and filling pore spaces. (*C*) Multiple magnetite crystals in single pore. (*D*) Example of moiré fringe data used to identify magnetite. (*E*) Dislocation loop with magnetite and ZrO_2 near recrystallization front (Fig. 3*E*). (*F*) Intersection of dislocation and pore demonstrating pipe diffusion of secondary Fe into pore spaces; *Insets* show Fe and Zr EDS maps. Mineral abbreviations: ilm, ilmenite; mag, magnetite. Images *A–D* from grain A; image *E* from grain B; images *D* and *F* are from additional grain C (*SI Appendix*, section A). Images *A–C,* grain A; image *E,* grain B; images *D* and *F,* grain C (*SI Appendix*, section A).

in grain B can be found in *SI Appendix*, Figs. S4–S6. Fig. 3 demonstrates the schematic progression of features seen in grain B (Fig. 3*A*). The initial zircon grain shows oscillatory zoning in CL, which reflects a variation in trace element content, e.g., U, and a high-U rim (Fig. 3*B*). Radiation damage slowly accumulates in the core, and the high-U rim becomes totally metamict. Partial annealing of the core results in linked pore-dislocation networks, and the high-U rim facilitates fluid ingress at a later stage, reorganizing the annealing microstructures (Fig. 3 *C* and *F* and *SI Appendix*, Fig. S5*A*). Magnetite growth in the core can only take place once this network of secondary features has accumulated (Fig. 3 *D*, *F*, and *G* and *SI Appendix*, Fig. S4 *A–D*), and must therefore significantly postdate zircon crystallization.

Clear identification of the Fe-oxide as magnetite is the result of correlating the various datasets. Fe-oxides observed chemically from STEM energy dispersive spectroscopy (EDS) were observed using moiré fringe lattice interference patterns between the zircon and oxide. The resultant moiré fringe d-spacing (Fig. 2*D* and *SI Appendix*, Fig. S11) defines the Fe-oxide as most likely magnetite, with a possibility of being maghemite. However, the paleomagnetic data showing complete NRM demagnetization by 580 °C means it is only possible for the inclusions to be magnetite (*SI Appendix*, Fig. S13). The extraction of robust Hadean paleomagnetic signals from zircon single crystals relies on the following assumptions about any given magnetic particle: (*i*) iron oxide grains became trapped as primary inclusions in igneous zircon; (*ii*) inclusions within the zircon acquired a primary TRM during postcrystallization cooling and have not been subsequently reheated above the Curie temperature; (*iii*) armoured magnetic inclusions remained chemically and thermally unaltered by pre- and postdepositional high-temperature metamorphic and low-temperature aqueous alteration/recrystallization events; and (*iv*) the high-temperature component of primary TRM can be separated from overlapping sources of secondary magnetization. If all these conditions are met, then the Jack Hills zircons have the potential to constrain the properties of the Hadean geodynamo. If any one of these conditions is violated, the case for primary magnetization cannot be made.

We have observed two pathways for the formation of secondary single-domain magnetite in Jack Hills zircon, circumventing criteria (*i*) and (*iii*) above. Formation of secondary magnetite in the presence of a magnetic field will generate a chemical remanent magnetization (CRM). An important property of CRM is that its thermal unblocking temperature is not limited by the temperature of its acquisition, but by the volume of the particles formed (26). Magnetite particles of sufficient size acquire CRM with laboratory unblocking temperatures that overlap with the 550–585 °C window attributed to primary Hadean remanence (27). A representative (but not exhaustive) summary of magnetite particles observed using TEM is given in *SI Appendix*, Table S1. Measurements of the length (L) and width (W) of each particle were taken directly from the TEM images. Fig. 4 compares the 2D projected lengths and

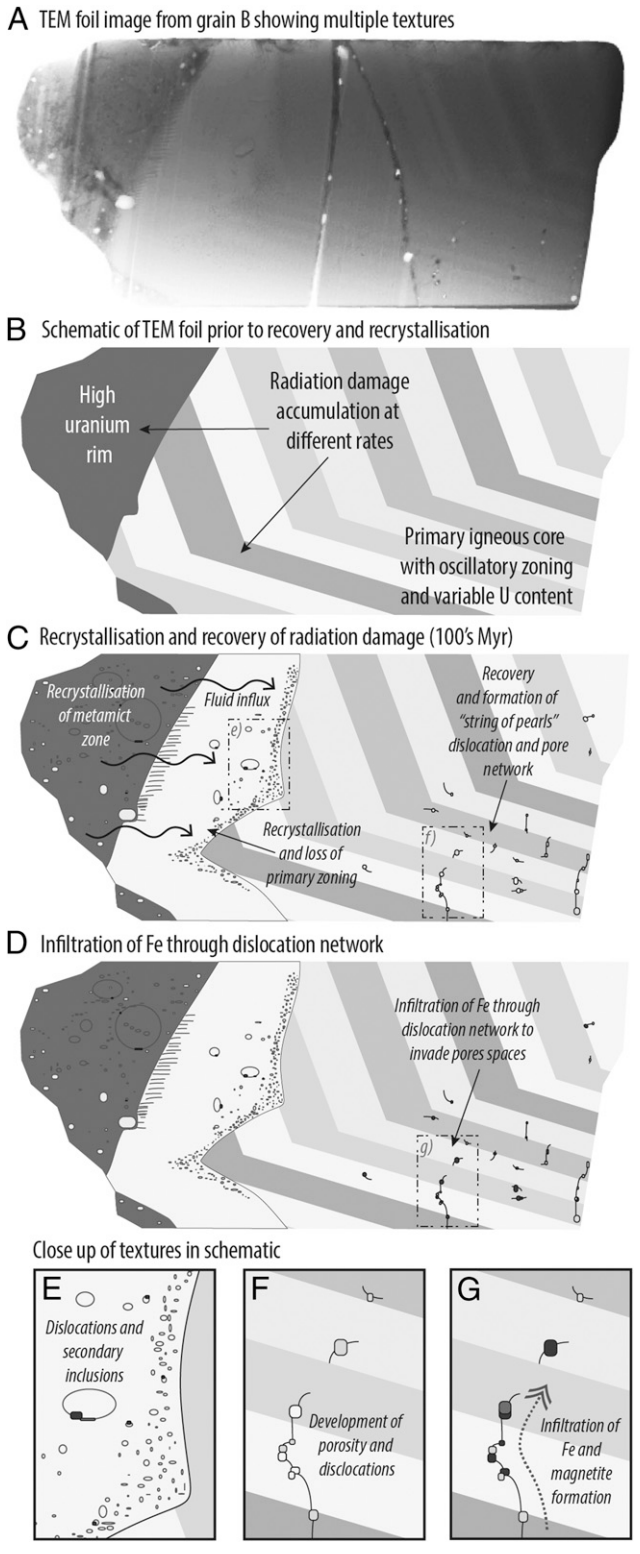

Fig. 3. Summary diagram showing order of events forming secondary inclusions in grain B. (*A*) TEM BF image of lamella. (*B*) Schematic of zoning in zircon. Oscillatory zoning with variable U content (light = low U) accumulating radiation damage at different rates. High-U rim area accumulates damage most rapidly. (*C*) Fluid-mediated recrystallization and fluid-absent recovery process occur 100s My after grain formation. (*D*) Fe infiltrates dislocation-pore network forming magnetite. (*E–G*) Close up of processes *Inset* areas in *C* and *D*. Features shown in *F* and *G* are clear in images from *SI Appendix*, Fig. S4 *A–D*.

aspects ratios of the observed particles with the calculated thresholds for superparamagnetic, single-domain, and vortex behavior in isolated magnetite particles (28). The majority of observed particles are predicted to be single domain (Fig. 4*A*), with 40% of grains having blocking temperatures >500 °C (Fig. 4*B*). Two of the largest particles observed are predicted to lie above the threshold for single-vortex behavior for noninteracting magnetite (28). Micromagnetic simulations confirm that these particles adopt either single-domain or single-vortex states at remanence, that both adopt vortex states during magnetization reversal, and that their blocking temperatures are 570–575 °C (*SI Appendix*, section D). Single-vortex particles of a similar size have been observed to retain their remanence all of the way to the Curie temperature (29). Thermal demagnetization of grain A demonstrates that 30–40% of its NRM is retained after heating to 550 °C in zero field and that the NRM is fully demagnetized by 580 °C (*SI Appendix*, section C), confirming the presence of magnetite remanence carriers with high blocking temperatures. This means that a putative primary Hadean TRM and secondary CRM would have overlapping blocking spectra, making it difficult to discriminate primary and secondary remanence, violating criteria (*iv*) above.

Given these observations of secondary ferromagnetism, recognizing the presence of (or demonstrating the lack of) secondary magnetite via high-resolution magnetic, compositional, and mineralogical analyses are now essential steps in the quest for Hadean paleomagnetism. Although most magnetite particles formed through fluid-mediated recrystallization that we observed fall well within the stable single-domain size range, their frequently low volumes yield blocking temperatures that mostly lie outside the 550–585 °C window used to isolate Hadean remanence. Therefore, CRM acquired via this mechanism might be avoided through careful sample characterization and thermal demagnetization to 550 °C (27). However, the formation of secondary magnetite in crystalline zircon via the pipe-diffusion mechanism cannot be recognized using CL imaging, is not associated with Pb loss, and produces magnetite particles with sizes and aspect ratios spanning the stable single-domain to single-vortex range, with blocking temperatures that fall within the 550–585 °C window.

Evaluation of the TEM images in this study enables an estimate to be made of the volume expansion of the crystal lattice due to radiation damage. Image analysis of the ratio of zircon to observed pore spaces shows a volume expansion of ∼0.7%, used as a proxy for lattice expansion, which can be converted to the time taken to accumulate this damage based on the original actinide content (30). Back-calculated U and Th concentrations give a lower estimate of c. 950 and c. 500 My for grains A and B, respectively, to produce the observed porosity (*SI Appendix*, section B provides more details). This means that the Fe source may be from fluid alteration within precursor igneous rocks, but also allows for the source of Fe to be the Jack Hills sediment itself, consistent with deep weathering estimates (31). This estimate provides an upper age limit for magnetite formation, and is clearly significantly later than zircon crystallization (Fig. 3).

The distinct possibility that the secondary Fe source predates sedimentation at 3.0 Ga is important, as it negates the use of microconglomerate tests on the Jack Hills sediments as evidence for primary magnetization. The observed radiation damage in Jack Hills zircon is much lower than that expected on the basis of their actinide content and age (32). Therefore, this pipe-diffusion mechanism is expected to be widespread, a natural consequence of the build up and subsequent recovery of radiation damage that will affect all ancient zircon crystals. Therefore, unless primary magnetite can be confirmed, the existence of a magnetic field during Eoarchean and Hadean remains an unknown.

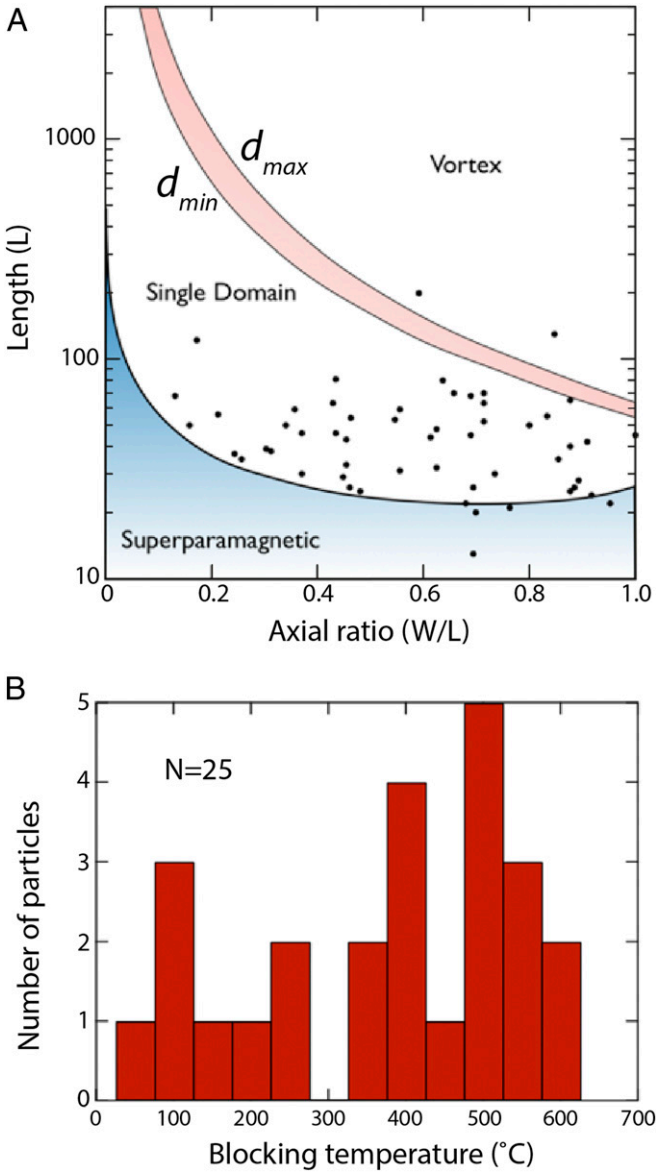

Fig. 4. Magnetic information on secondary magnetite particles observed in Jack Hills zircon. (*A*) *L* vs. aspect ratio (*W*/*L*) for magnetite particles observed using TEM (*SI Appendix*, Table S1). Boundaries between superparamagnetic, single-domain, and vortex states are based on micromagnetic simulations of noninteracting magnetite (28). (*B*) Histogram of calculated blocking temperatures (50 °C bin width), excluding SP particles. Blocking temperatures were calculated for laboratory observation times (taken to be t_{obs} = 100 s). A significant number of the particles observed have T_B > 500 °C, consistent with the rapid loss of NRM observed using superconducting quantum interference device (SQUID) magnetometry (*SI Appendix*, Fig. S13).

Methods

SEM. An FEI Quanta 650 field emission gun SEM was used to collect both energy dispersive spectroscopy elemental maps (at 20 kV accelerating voltage), backscattered electron (BSE), and cathodoluminescence micrographs (collected at 5 kV). The BSE and CL maps were collected in parallel, and the EDS maps were collected subsequently. EDS maps were collected using two Bruker 6|30 EDS detectors simultaneously to increase the overall counts and improve throughput. For grain C, each pixel's spectrum was denoised using a Python-based nonnegative matrix factorization algorithm, background subtracted, and then peak integration performed on the $Fe_{k\alpha}$ window of 6.0–6.7 keV (33, 34).

TEM. The TEM specimen was site-precisely prepared from a zircon grain using a dual beam focused ion beam (FIB) scanning electron microscope field electron and ion (FEI), now Thermo Fisher Scientific, Helios NanoLab. An in situ lift-out technique was applied to extract and transfer the specimen onto a standard TEM molybdenum half grid, and a platinum bar was deposited on the surfaces of target areas before FIB processing. The TEM lamella was made with the reduced FIB voltages down to ∼2–5 kV to minimize FIB-induced damage (35), and was cleaned for about 3–5 min in a plasma chamber before being loaded into the TEM microscope. The TEM study was carried out using two microscopes: FEI Tecnai Osiris and FEI Titan^3 (80–300 kV), and both were dedicated to scanning TEM operation. The Osiris microscope fitted with four silicon drift detectors for energy dispersive X-ray spectrometry analysis was used for STEM high-angle annular dark field (HAADF) and STEM-bright field (BF) imaging and fast STEM chemical mapping operating at 200 kV. The Titan microscope had a probe-forming corrector for spherical aberration, allowing for high resolution imaging in STEM configuration at 300 kV. To obtain optimum contrast for identifying nanometer-sized particles, the STEM imaging was typically taken at the combination of the camera length between 80 and 250 mm and the screen currents of 0.05–0.3 nA; whereas, the STEM chemical mapping was performed at the screen currents larger than about 0.1 nA.

U–Pb Geochronology. Grains were prescreened for ancient Pb isotope signatures on the CAMECA ims1270 ion microprobe using a 15-nA O-primary beam and a mass resolution of 5000. This used more rapid count times to analyze a large number of grains but at lower than normal precision. Oxygen flooding to c. 1 × 10-5 torr was used to enhance Pb ionization. Following a 2-min presputter to clean the zircon surface, Pb isotopes were counted for 30 s in monocollection mode. During a later session, U–Pb ages were measured under the more typical instrumental conditions and count times, using the AS3 zircon standard (36) for Pb/U relative sensitivity factor calibration. More details on the U–Pb method can be found in Quidelleur et al. (37).

QDM. We use the quantum diamond microscope at the Harvard Paleomagnetics Laboratory to obtain high-resolution magnetic field maps of zircon grains A and B (Fig. 1 *C* and *G*). Both grains are first subjected to a 0.25 T isothermal remanent magnetization oriented out of the imaging plane. The polished surface of the zircons is then placed in contact with the sensing diamond, which has nitrogen-vacancy (*N*-V) centers implanted uniformly in a 4-μm layer. We then optically excite the (*N*-V) centers with a 500-mW 532-nm wavelength laser and image the fluorescence at a spatial resolution of 1.17 μm per pixel. To maximize the signal-to-noise ratios, we perform the experiments in projective magnetic microscopy mode (18) that directly measures the magnetic field projection in the [111] direction of the diamond lattice. This protocol involves two measurements taken under bias fields of 900 μT oriented in opposing directions parallel to the [111] axis. The two maps are then summed to isolate the ferromagnetic component. The reversal accuracy of the bias field is 1 part in 1500, resulting in a residual bias field of 600 nT, which is then subtracted from the summed map. The residual bias field in the final map is therefore at least 10^3 smaller than the zircon signals and can be neglected. We then convert these projected magnetic field values to the magnetic field perpendicular to the measurement plane using spectral domain algorithm (38).

Laser Ablation. U and Th measurements were made for the zircon grains alongside the TEM locations to calculate radiation damage times. Analyses were carried out using an ESI UP193UC laser system coupled to a Perkin–Elmer Nexion 350D inductively coupled plasma mass spectrometer (LA-ICP-MS) in the Department of Earth Sciences at the University of Cambridge. The LA-ICP-MS data acquisition settings were 1 sweep per reading, 80 readings, 1 replicate, and total data acquisition lasted 50 s (∼1 data point for each element per second). The instrument was set up for background data followed by ablation for 20 s, at a rep rate of 10 Hz, and power on the sample of ∼3 joules per cm^2. Data were processed using Iolite software with the trace element DRS (39), with concentrations calibrated against KLDF standard zircon (Curtin University internal standard; U 507 ppm, Th 75 ppm) and 91500 (40). National Institute of Standards and Technology glasses SRM 610 and 612 (41) were run to monitor instrument stability. U and Th concentrations were calculated for the crystallization ages of the grains.

ACKNOWLEDGMENTS. We thank two anonymous reviewers for their constructive comments that greatly improved the manuscript. The research leading to these results has received funding from the European Research Council under the European Union's Seventh Framework Programme (Grant FP/2007-2013)/European Research Council Grant Agreement 320750, Natural Environment Research Council Grant NE/P002498/1, National Science Foundation (NSF) Grant EAR1647504, and Thomas F. Peterson, Jr. The University of California, Los Angeles ion microprobe facility is partly supported by a grant from the Instrumentation and Facilities Program, Division of Earth Sciences, NSF (1339051).

1. Tarduno JA, et al. (2010) Geodynamo, solar wind, and magnetopause 3.4 to 3.45 billion years ago. *Science* 327:1238–1240.
2. Biggin AJ, et al. (2011) Palaeomagnetism of Archaean rocks of the Onverwacht Group, Barberton greenstone belt (southern Africa): Evidence for a stable and potentially reversing geomagnetic field at ca. 3.5Ga. *Earth Planet Sci Lett* 302:314–328.
3. McElhinny M, Senanayake W (1980) Paleomagnetic evidence for the existence of the geomagnetic field 3.5 Ga ago. *J Geophys Res Solid Earth* 85:3523–3528.
4. Gomi H, et al. (2013) The high conductivity of iron and thermal evolution of the Earth's core. *Phys Earth Planet Inter* 224:88–103.
5. Pozzo M, Davies C, Gubbins D, Alfè D (2013) Transport properties for liquid silicon-oxygen-iron mixtures at Earth's core conditions. *Phys Rev B* 87:014110.
6. Ohta K, Kuwayama Y, Hirose K, Shimizu K, Ohishi Y (2016) Experimental determination of the electrical resistivity of iron at Earth's core conditions. *Nature* 534: 95–98.
7. Davies C, Pozzo M, Gubbins D, Alfè D (2015) Constraints from material properties on the dynamics and evolution of Earth's core. *Nat Geosci* 8:678–685.
8. O'Rourke JG, Korenaga J, Stevenson DJ (2017) Thermal evolution of Earth with magnesium precipitation in the core. *Earth Planet Sci Lett* 458:263–272.
9. Badro J, Siebert J, Nimmo F (2016) An early geodynamo driven by exsolution of mantle components from Earth's core. *Nature* 536:326–328.
10. Konôpková Z, McWilliams RS, Gómez-Pérez N, Goncharov AF (2016) Direct measurement of thermal conductivity in solid iron at planetary core conditions. *Nature* 534:99–101.
11. Tarduno JA, Cottrell RD, Davis WJ, Nimmo F, Bono RKA (2015) PALEOMAGNETISM. A Hadean to Paleoarchean geodynamo recorded by single zircon crystals. *Science* 349: 521–524.
12. Valley JW, et al. (2014) Hadean age for a post-magma-ocean zircon confirmed by atom-probe tomography. *Nat Geosci* 7:219–223.
13. Fu RR, et al. (2017) Evaluating the paleomagnetic potential of single zircon crystals using the Bishop Tuff. *Earth Planet Sci Lett* 458:1–13.
14. Weiss BP, et al. (2018) Secondary magnetic inclusions in detrital zircons from the Jack Hills, Western Australia, and implications for the origin of the geodynamo. *Geology* 5: 427–430.
15. Weiss BP, et al. (2015) Pervasive remagnetization of detrital zircon host rocks in the Jack Hills, Western Australia and implications for records of the early geodynamo. *Earth Planet Sci Lett* 430:115–128.
16. Maas R, Kinny PD, Williams IS, Froude DO, Compston W (1992) The Earth's oldest known crust: A geochronological and geochemical study of 3900-4200 Ma old detrital zircons from Mt. Narryer and Jack Hills, Western Australia. *Geochim Cosmochim Acta* 56:1281–1300.
17. Wilde SA, Valley JW, Peck WH, Graham CM (2001) Evidence from detrital zircons for the existence of continental crust and oceans on the Earth 4.4 Gyr ago. *Nature* 409: 175–178.
18. Glenn DR, et al. (2017) Micrometer-scale magnetic imaging of geological samples using a quantum diamond microscope. *Geochem Geophys Geosyst* 18:3254–3267.
19. Piazolo S, et al. (2016) Deformation-induced trace element redistribution in zircon revealed using atom probe tomography. *Nat Commun* 7:10490.
20. Timms NE, Reddy SM, Gerald JDF, Green L, Muhling JR (2012) Inclusion-localised crystal-plasticity, dynamic porosity, and fast-diffusion pathway generation in zircon. *J Struct Geol* 35:78–89.
21. White LF, et al. (2017) Atomic-scale age resolution of planetary events. *Nat Commun* 8:15597.
22. Geisler T, Schaltegger U, Tomaschek F (2007) Re-equilibration of zircon in aqueous fluids and melts. *Elements* 3:43–50.
23. Geisler T, Pidgeon RT, Kurtz R, van Bronswijk W, Schleicher H (2003) Experimental hydrothermal alteration of partially metamict zircon. *Am Mineral* 88:1496–1513.
24. Lappe S-CLL, et al. (2011) Mineral magnetism of dusty olivine: A credible recorder of pre-accretionary remanence. *Geochem Geophys Geosyst* 12:Q12Z35.
25. Einsle JF, et al. (2016) Multi-scale three-dimensional characterization of iron particles in dusty olivine: Implications for paleomagnetism of chondritic meteorites. *Am Mineral* 101:2070–2084.
26. McClelland-Brown E (1982) Discrimination of TRM and CRM by blocking-temperature spectrum analysis. *Phys Earth Planet Inter* 30:405–414.
27. Tarduno JA, Cottrell RD (2013) Signals from the ancient geodynamo: A paleomagnetic field test on the Jack Hills metaconglomerate. *Earth Planet Sci Lett* 367:123–132.
28. Muxworthy AR, Williams W (2009) Critical superparamagnetic/single-domain grain sizes in interacting magnetite particles: Implications for magnetosome crystals. *J R Soc Interface* 6:1207–1212.
29. Almeida TP, et al. (2016) Direct visualization of the thermomagnetic behavior of pseudo-single-domain magnetite particles. *Sci Adv* 2:e1501801.
30. Murakami T, Chakoumakos BC, Ewing RC, Lumpkin GR, Weber WJ (1991) Alpha-decay event damage in zircon. *Am Mineral* 76:1510–1532.
31. Pidgeon RT, Nemchin AA, Whitehouse MJ (2017) The effect of weathering on U–Th–Pb and oxygen isotope systems of ancient zircons from the Jack Hills, Western Australia. *Geochim Cosmochim Acta* 197:142–166.
32. Pidgeon R (2014) Zircon radiation damage ages. *Chem Geol* 367:13–22.
33. Lee DD, Seung HS (1999) Learning the parts of objects by non-negative matrix factorization. *Nature* 401:788–791.
34. de la Peña F, et al. (2017) Data from "hyperspy/hyperspy: HyperSpy 1.1.2." Zenodo. Available at https://zenodo.org/record/240660.
35. Tang F, et al. (2018) Nanoscale structural and chemical analysis of F-implanted enhancement-mode InAlN/GaN heterostructure field effect transistors. *J Appl Phys* 123:024902.
36. Paces JB, Miller JD (1993) Precise U-Pb ages of Duluth complex and related mafic intrusions, northeastern Minnesota: Geochronological insights to physical, petrogenetic, paleomagnetic, and tectonomagmatic processes associated with the 1.1 Ga midcontinent rift system. *J Geophys Res Solid Earth* 98:13997–14013.
37. Quidelleur X, et al. (1997) Thermal evolution and slip history of the Renbu Zedong Thrust, southeastern Tibet. *J Geophys Res Solid Earth* 102:2659–2679.
38. Lima EA, Weiss BP (2009) Obtaining vector magnetic field maps from single-component measurements of geological samples. *J Geophys Res Solid Earth* 114: B06102.
39. Paton C, Hellstrom J, Paul B, Woodhead J, Hergt J (2011) Iolite: Freeware for the visualisation and processing of mass spectrometric data. *J Anal At Spectrom* 26: 2508–2518.
40. Wiedenbeck M, et al. (2004) Further characterisation of the 91500 zircon crystal. *Geostand Geoanal Res* 28:9–39.
41. Pearce NJG, et al. (1997) A compilation of new and published major and trace element data for NIST SRM 610 and NIST SRM 612 glass reference materials. *Geostand Newsl* 21:115–144.